The Astrophysical Journal, 901:148 (7pp), 2020 October 1 https://doi.org/10.3847/1538-4357/abb2a7

Observations and Modeling of the Onset of Fast Reconnection in the Solar Transition Region

L. Guo-J. Guo[1,2], Bart De Pontieu[1,3,4], Y.-M. Huang[5,6], H. Peter[6,7], and A. Bhattacharjee[5,6]
[1] Lockheed Martin Solar & Astrophysics Laboratory, 3251 Hanover St., Palo Alto, CA 94304, USA; bdp@lmsal.com
[2] Bay Area Environmental Research Institute, NASA Research Park, Moffett Field, CA 94035, USA
[3] Rosseland Center for Solar Physics, University of Oslo, P.O. Box 1029 Blindern, NO-0315 Oslo, Norway
[4] Institute of Theoretical Astrophysics, University of Oslo, P.O. Box 1029 Blindern, NO-0315 Oslo, Norway
[5] Center for Heliophysics, Princeton Plasma Physics Laboratory, Princeton University, Princeton, NJ 08544, USA
[6] Max-Planck-Princeton Center for Plasma Physics, Princeton, NJ 08540, USA
[7] Max Planck Institute for Solar System Research, Justus-von-Liebig-Weg 3, D-37077 Göttingen, Germany
Received 2020 June 26; revised 2020 August 21; accepted 2020 August 24; published 2020 October 5

Abstract

Magnetic reconnection is a fundamental plasma process that plays a critical role not only in energy release in the solar atmosphere, but also in fusion, astrophysics, and other space plasma environments. One of the challenges in explaining solar observations in which reconnection is thought to play a critical role is to account for the transition of the dynamics from a slow quasi-continuous phase to a fast and impulsive energetic burst of much shorter duration. Despite the theoretical progress in identifying mechanisms that might lead to rapid onset, a lack of observations of this transition has left models poorly constrained. High-resolution spectroscopic observations from NASA's Interface Region Imaging Spectrograph now reveal tell-tale signatures of the abrupt transition of reconnection from a slow phase to a fast, impulsive phase during UV bursts or explosive events in the Sun's atmosphere. Our observations are consistent with numerical simulations of the plasmoid instability, and provide evidence for the onset of fast reconnection mediated by plasmoids and new opportunities for remote-sensing diagnostics of reconnection mechanisms on the Sun.

Unified Astronomy Thesaurus concepts: Solar transition region (1532); Solar chromosphere (1479); Solar magnetic reconnection (1504); Solar magnetic fields (1503)

1. Introduction

Magnetic reconnection is a process in which the magnetic topology is changed and magnetic energy is released to heat plasma, drive Alfvénic flows, induce Alfvén as well as magnetoacoustic waves, and energize particles. It is responsible for energetic phenomena such as geomagnetic storms and aurora (Lui 1996; Sitnov et al. 2019), solar flares and coronal mass ejections (Tsuneta 1996; Kliem et al. 2000; Lin & Forbes 2000; Karlický & Bárta 2007; Shibata & Magara 2011; Li et al. 2016), X-ray flares in magnetars (Hurley et al. 2005), and magnetic interactions between neutron stars and their accretion disks (Kato et al. 2004). It is also crucially important in laboratory plasma physics because it triggers the sawtooth crashes that can potentially cause disruptive instability in magnetically confined fusion plasmas (Taylor 1986; Bhattacharjee et al. 2001; Yamada et al. 2010). A better understanding of reconnection is thus a common challenge confronting laboratory, space, and astrophysical plasma physicists.

Recently, observational and experimental works have provided new insights into reconnection mechanisms. For example, NASA's Magnetospheric Multiscale Mission has found direct evidence for electron demagnetization and acceleration at reconnection sites in Earth's magnetosphere (Burch et al. 2016), while laboratory experiments have revealed structures in the diffusion region that trigger fast reconnection (Ji et al. 2004; Katz et al. 2010; Dorfman et al. 2013). Observations from the Cluster spacecraft in the Earth's magnetotail (Chen et al. 2008) and more recently the Parker Solar Probe have found magnetic islands in the inner solar wind (Howard et al. 2019). However, many questions remain about how the onset of fast reconnection occurs. For example, transition region explosive events, rapid brightenings thought to be driven by reconnection and associated with strong flows visible in spectral lines formed at temperatures of a few hundred thousand kelvin (Brueckner 1981; Dere et al. 1989), occur on timescales of minutes, much shorter than classic reconnection mechanisms predict. Recent progress in reconnection theory (Shibata & Tanuma 2001; Loureiro et al. 2007; Bhattacharjee et al. 2009) suggests that under certain circumstances fast reconnection can be triggered by the so-called plasmoid instability when a thin current sheet breaks up into secondary current sheets and plasmoids (or magnetic islands). Recent theoretical studies (e.g., Pucci & Velli 2013; Comisso et al. 2016; Uzdensky & Loureiro 2016; Huang et al. 2017) suggest that the thinning of the current sheet and growth of various tearing modes proceed simultaneously before fast reconnection is triggered. Nevertheless, these predictions for the onset of the fast reconnection, namely a transition from a slow quasi-continuous phase to fast, plasmoid-mediated, reconnection, have not yet found definitive support from observations, despite observations of the presence of plasmoid-like features (Lin et al. 2005; Singh et al. 2012; Takasao et al. 2012; Rouppe van der Voort et al. 2017). In addition, alternative theories have suggested that strong turbulent motions in solar microflares lead to the onset of fast reconnection (Chitta & Lazarian 2020).

UV bursts, sudden and compact brightenings in UV light, provide an opportunity to study magnetic reconnection on the Sun (Young et al. 2018). A variety of phenomena such as transition region explosive events and Interface Region Imaging Spectrograph (IRIS) bombs are considered to be UV bursts: we shall refer to all these events as UV bursts in this paper. These bursts are often characterized by broad spectral line profiles and

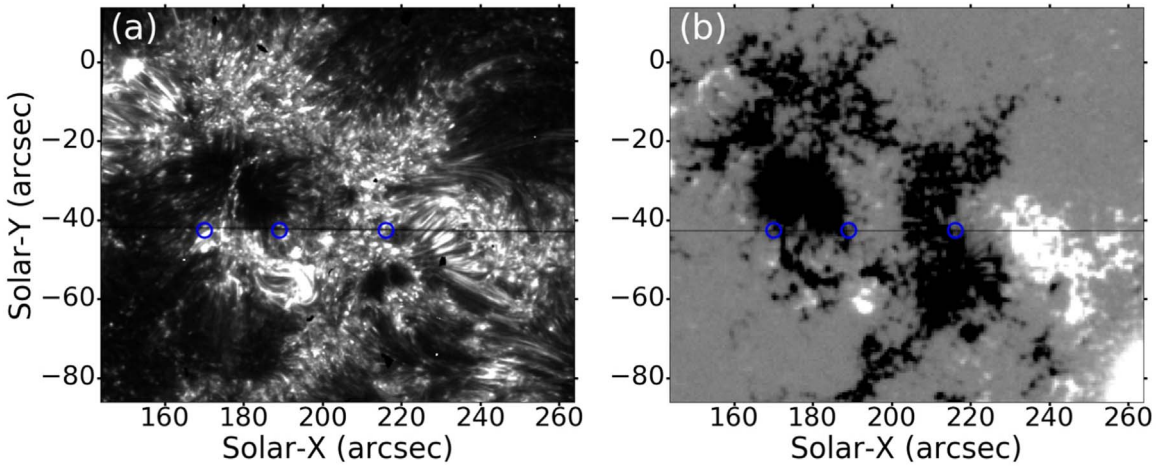

Figure 1. UV bursts occur in regions of strong magnetic activity. Active Region 12036 on 2014 May 05 13:22:21 UT: (a) IRIS 1400 slit-jaw image in a wavelength range around 1400 Å showing mainly 80,000 K plasma; (b) HMI line-of-sight magnetogram showing the distribution of magnetic field on the solar surface. The black horizontal line in (a) and (b) is the IRIS spectrometer slit, the blue O' signs mark locations of UV bursts. When observed at sufficiently high spatial resolution and magnetic sensitivity (i.e., higher than displayed here), these bursts are often located where opposite magnetic polarities meet.

the more violent ones show a strong enhancement of emission (Dere et al. 1991). They are thought to be driven by magnetic reconnection (Dere et al. 1991; Peter et al. 2014; Innes et al. 1997), because of their characteristic spectral profiles that indicate strong bidirectional flows, which typically occur where magnetic flux concentrations of opposite polarity meet (Hansteen et al. 2019). Other explanations for explosive events exist as well (Curdt & Tian 2011; Curdt et al. 2012), but the majority of explosive events are still considered to be driven by reconnection. As mentioned, high-resolution observations of UV bursts have provided tantalizing indications for the presence of plasmoids (Rouppe van der Voort et al. 2017), but they have not shown the transition from a slow to fast phase. In this paper we present observational evidence for such a transition and compare it with numerical simulations of magnetic reconnection, transitioning from a slow phase to a plasmoid-mediated phase in which reconnection occurs much faster.

In Section 2 we describe the observations, while we provide details of the numerical simulations in Section 3. Our results are described in Section 4 and we finish with a discussion and conclusions in Section 5.

2. Observations

IRIS is a NASA small explorer that contains a high-resolution spectrograph and slit-jaw imager, both sensitive to near- and far-UV light. The instrument has spectral passbands that cover emission lines and continua that originate at temperatures covering the solar atmosphere from the photosphere to the corona (De Pontieu et al. 2014). In this paper, we concentrate on the Si IV 1403 Å line originating in the transition region between the chromosphere and corona at about 80,000 K. The spatial resolution of IRIS is 0.″33, while the spectral sampling corresponds to a velocity sampling of around 2.7 km s^{-1}. We also use the slit-jaw images of the 1400 Å passband from the IRIS slit-jaw imager, which are dominated by the Si IV lines at 1394 and 1403 Å as well as the far-ultraviolet continuum (De Pontieu et al. 2014). We analyzed four IRIS data sets (so-called sit-and-stare rasters) to search for UV bursts sharing similar spectral properties: 2013 August 13 at 13:35 UTC, 2014 February 4 at 00:29 UTC, 2014 April 15 09:59 UTC, and 2014 May 4 12:09 UTC. These data sets have cadences short enough (3 s for all, except for the latter, which has 5 s cadence) to observe fast-evolving UV bursts. All were targeted on active regions.

We also use a magnetogram obtained by the Helioseismic and Magnetic Imager (HMI; Scherrer et al. 2012) on board the Solar Dynamics Observatory (SDO; Pesnell et al. 2012) along with an IRIS slit-jaw image to show an active region with several UV bursts in Figure 1, with sample spectra shown in Figure 2. Coalignment of the HMI and IRIS data was done by cross-correlation between the 1600 Å continuum obtained by the Atmospheric Imaging Assembly (AIA; Lemen et al. 2012) on board SDO and IRIS 2796 Å slit-jaw images that show the chromosphere in the Mg II k line. We first perform coalignment using the coordinates provided in the headers of the data sets and then use a cross-correlation method to determine the pointing offset between the IRIS telescope and the AIA telescope. The HMI and AIA data are both full-disk and easily coaligned.

3. Simulations

The simulations in this article solve single-fluid, resistive MHD equations with anisotropic heat conduction and radiative cooling, using a state-of-the-art simulation code (Huang et al. 2017). Similar to Innes et al. (2015), we use a Harris sheet equilibrium as the initial configuration, which is given by $B_x(y) = B_0 \tanh(y/\delta)$ (Harris 1962), where $\delta = 10$ km is the half width of the current sheet; we adopt a Lundquist number of 10^5, which is defined by $S = Lv_A / \eta$, where L the spatial scale, v_A is the Alfvén speed, and η is the resistivity. We adopt the radiative loss estimated in Colgan et al. (2008). Assuming the simulation domain is in thermal equilibrium initially, background heating is added to balance the radiative loss at $t = 0$ s. The resistive MHD equations are solved in a two-dimensional domain 2 Mm × 2 Mm on a grid of 2064 × 2048 grid points. In Figure 3 we show a subdomain enclosing the current sheet (<1 Mm) instead of the whole simulation domain. The x direction is along the long axis of the current sheet and the y-direction is perpendicular to the current sheet. Viscosity is not included in this qualitative study. Initially, at the asymptotic

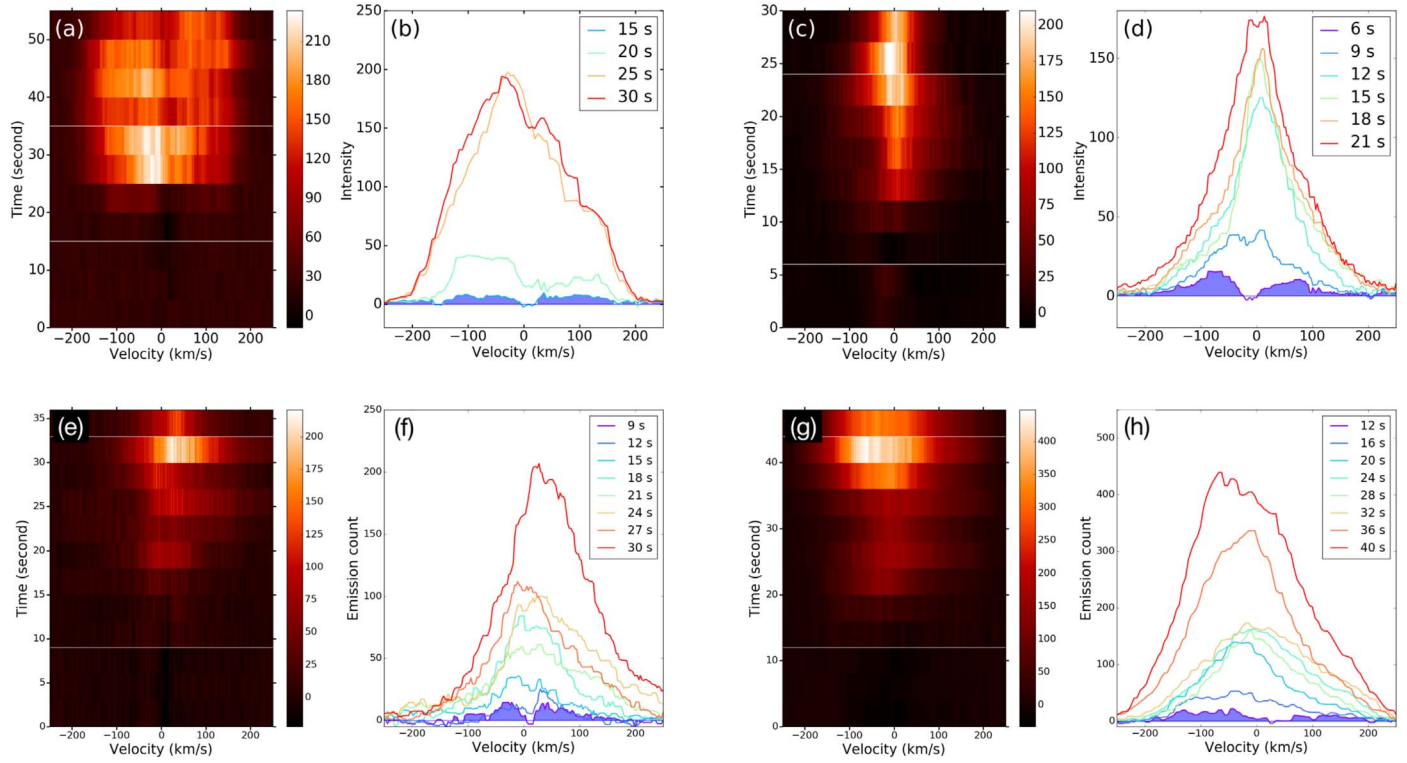

Figure 2. IRIS observations of UV bursts indicate the onset of fast reconnection. Panel (a): time evolution of Si IV spectra at the beginning of the event. Panel (b): spectral line profiles for selected times in the time range highlighted by white horizontal lines in panel (a). Panels (c), (d), (e), (f), (g), and (h) show similar evolution for three other events. All four events show transitions from low-intensity, double-peak shaped line profiles to high-intensity, triangle shaped line profiles. In panels (b), (d), (f), and (h) the line profile at the first time step is shaded in blue to accentuate its double-peak shape.

region, the Alfvén speed is 200 km s^{-1}, the number density is 10^{10} cm^{-3}, the temperature is 3×10^4 K, and the plasma beta = 0.1. We did not include gravity and a stratified atmosphere in the current study. The fact that the spatial extent of a UV burst, and thus our computational domain, is smaller than the pressure scale height in the transition region at around 100,000 K justifies this assumption. Gravity and stratification would cause a density gradient along the outflow direction and possibly decrease the speed of reconnection outflows toward the Sun and slightly alter the red wings of line profiles. Nevertheless, we do not expect that including these two terms will qualitatively change our results.

Note that the simulation is conducted over a relatively narrow range of plasma parameters, which are chosen specifically to focus on the observed events in the temperature range of Si IV formation. The initial temperature is chosen to be 30,000 K so that the current sheet is at the lower range of the Si IV contribution function (weaker emission) in the slow phase and at the peak of the Si IV contribution function (stronger emission) in the fast phase. If we use lower initial temperatures (e.g., 10,000 K), the slow phase is less visible in Si IV but the emission in the fast phase will still be strong. It certainly is possible to imagine other scenarios in which the slow phase is too cool to be visible in the Si IV passband, the setup of our simulation in this paper is focused on UV bursts observed in Si IV with both phases visible.

4. Results

4.1. Observations of Onset of Fast Reconnection

A large number of UV bursts are observed in the four data sets. We use a feature-detection code to select line profiles with large line width and intensity, and filter out asymmetric line profiles, which are likely caused by events that are spread over several resolving elements of IRIS and would complicate analysis. Another advantage of selecting symmetric line profiles is that they are compatible with the choice of the line-of-sight direction along the outflows and our assumption of the numerical domain being enclosed within one IRIS pixel. Among all the events that satisfy the above criteria, we pick events with visibly sharp onsets, judging from changes of intensity and line width. Following the above selection criteria, we have found eight events in our data sets, of which we show four in Figure 2.

For events from data sets with short exposure times, line profiles can be noisy due to a low signal-to-noise ratio. In this case, we run a four-point averaging in the spatial and spectral dimensions to reduce the noise level in the data. To enhance the visibility of any signals immediately preceding the bright UV bursts, we subtract a line profile that is averaged over 10 time steps before the onset of the event to remove emission contributions from unrelated events that are either along the line of sight, or introduced by scattered light from neighboring pixels.

A few examples of UV bursts in the Si IV 1400 Å and their locations overplotted on the photospheric magnetogram are shown in Figure 1. These events hold the key in revealing the dynamics of reconnection sites and because transition region emission typically forms in a small volume, line-of-sight superposition, a common issue with observations in optically thin lines in the solar atmosphere, is much less of a challenge for such emissions. Here we report on IRIS observations of UV bursts in the Si IV 1400 Å line showing rapidly evolving spectra

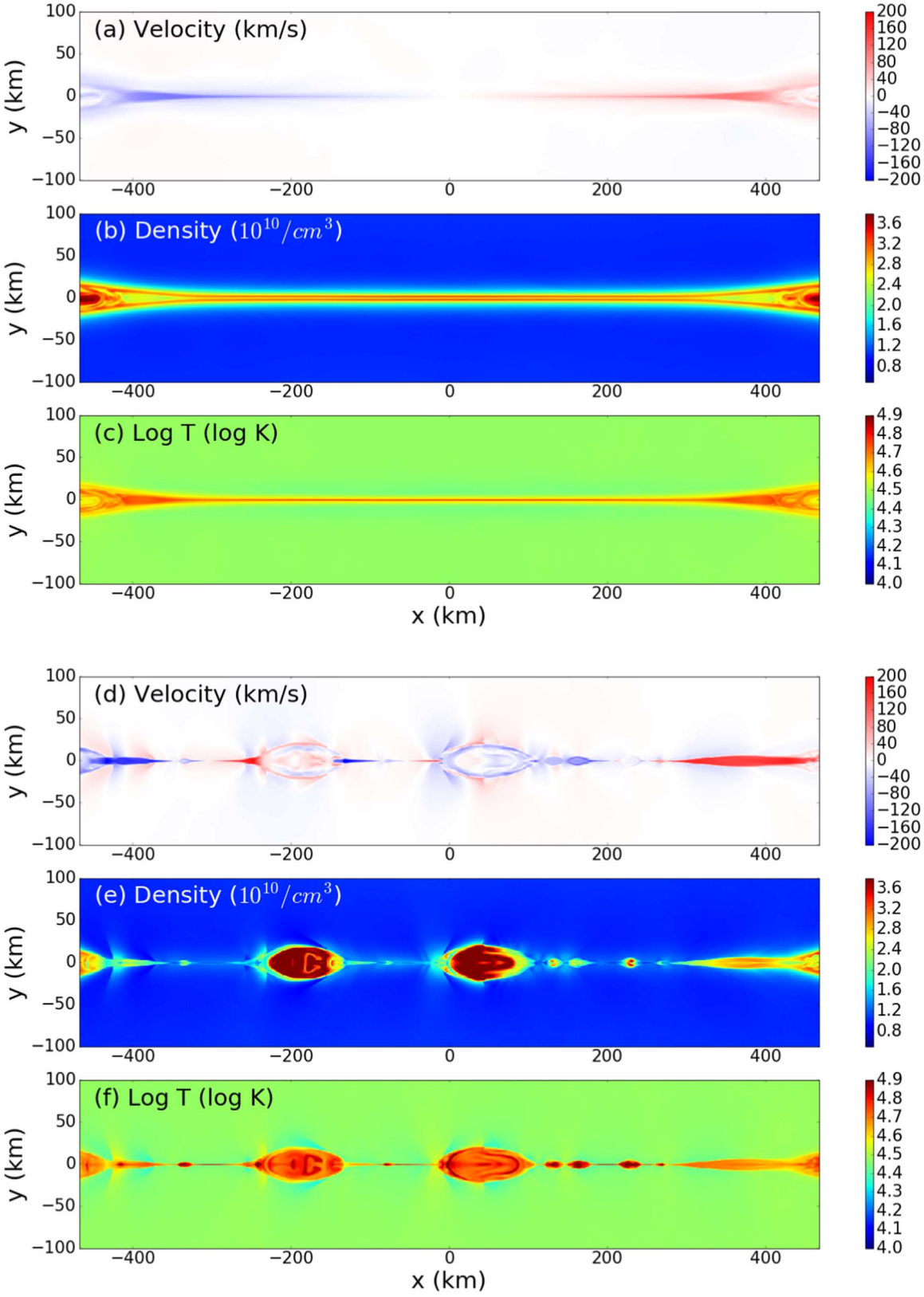

Figure 3. A numerical simulation shows the transition from slow reconnection (left) to fast reconnection mediated by plasmoids (right). Panels (a), (b), and (c): velocity, density, and temperature during the slow phase. Panels (d)–(f) show the same during the fast phase. Please note that the aspect ratio is enhancing the distance in the *y*-direction. The domain shown here covers about 1 Mm by 0.2 Mm, while the entire simulation domain covers 2 Mm by 2 Mm. The time between these two snapshots of the slow ($t = 4$ s in Figure 4) and the fast phases ($t = 10$ s in Figure 4) is only 6 s.

that indicate the onset of fast reconnection. Four examples are shown in Figure 2. Panel (a) shows the time evolution of the Si IV spectra observed during the first event. A sharp increase of intensity and width of spectra is visible at $t = 25$ s, which indicates the beginning of the impulsive phase of reconnection. Most interestingly, weak emission lasting two time steps is

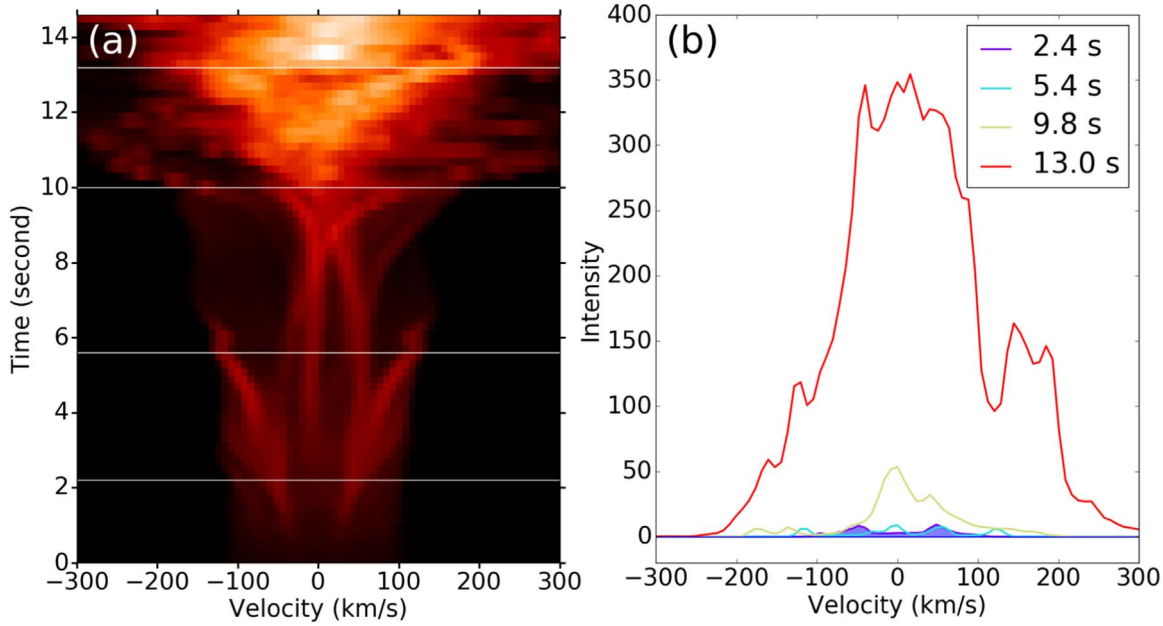

Figure 4. Synthesized Si IV spectra from the model agree well with IRIS observations. Panel (a) shows the time evolution of Si IV spectra synthesized from the reconnection model. Panel (b) shows the line profiles of the time steps marked by white horizontal lines in panel (a). These synthetic line profiles compare well in a qualitative sense with the observations shown in Figure 2, even though panel (a) is richer in structure here in the simulation than in the observations (Figures 2(a)–(c)), which is because of the higher resolution of the numerical model.

observed before $t = 25$ s, revealing activity preceding the onset of the impulsive phase. The intensity of line profiles at $t = 15$ and $t = 20$ is much weaker than line profiles at $t = 25$ and t = 30, suggesting that before the impulsive phase, heating is weaker than during the impulsive phase. Panel (b) of Figure 2 shows line profiles from $t = 15$ s to $t = 30$ s, with their positions marked by white lines in panel (a), showing more details of the evolution of line profiles. At $t = 15$, the observed line profiles exhibit double peaks (see the area shaded in blue), which can be produced by the bidirectional outflows expected from single-X-point reconnection (Innes et al. 1997). The low intensity at $t = 15$ s indicates weak activity, suggesting the single-X-point reconnection proceeds at a slow rate. In the impulsive phase, the most commonly observed line profiles are triangular line profiles with wide wings and a strong central component at the rest wavelength of Si IV, which we suggest is caused by fast reconnection mediated by plasmoids (Innes et al. 2015). The impact of plasmoids on the observed spectra has also been discussed by Hara et al. (2011) and Rouppe van der Voort et al. (2017). Panel (c) and panel (d) show the evolving line profiles for the second event, whose line profiles undergo evolution similar to the first event but exhibit more temporal snapshots during the lifespan of the event. We examined four different IRIS data sets of active regions and found another six cases showing similar properties. Two of those cases are shown in panels (e), (f), (g), and (h).

4.2. Numerical Modeling of Reconnection in Transition Region

In order to better interpret observations of UV bursts, we simulate a thinning current sheet with plasma parameters as close to that of the transition region as presently enabled by a state-of-the-art simulation code (Huang et al. 2017). In this simulation, the current sheet gradually thins down as multiple tearing modes slowly grow within it. When the islands produced by the most dominant mode disrupt the formation of the current sheet, the reconnection dynamics make a transition from the slowly evolving stage to rapid onset (Comisso et al. 2016; Uzdensky & Loureiro 2016; Huang et al. 2017, 2019; Peter et al. 2019). Panels (a)–(c) of Figure 3 show the velocity, density, and temperature of the current sheet during the slow phase, when the current sheet is dominated by an Alfvénic, bidirectional jet. The bidirectional jet weakens when plasmoids start to appear in the current sheet. As the plasmoids grow and coalesce, a substantial amount of plasma is trapped in the plasmoids (see the density in panel (e) of Figure 3 during the fast phase), some of which moves at slow velocities, compared to plasma in the secondary current sheet that mostly moves at Alfvénic speeds (see the velocity in panel (d) during the fast phase). As a result of the cascade of plasmoid formation, the velocity distribution in the current sheet assumes a wide range of values as well. With the velocity, density, and temperature distribution from the simulation, we are able to calculate the Si IV spectra of the simulated current sheet. The synthetic Si IV spectra are shown in Figure 4. In Figure 4(a), from $t = 0$ s to $t = 4$ s, the current sheet is in a slow phase when only spectra with very weak intensity are produced by the current sheet. Typical line profiles (Figure 4(b)) during this phase show a double-peak shape, with blue- and redshifted components at about 200 km s^{-1}, corresponding to a bidirectional jet at Alfvén velocity (Figure 3(a)). Starting from $t = 4$ s, plasmoids start to appear in the current sheet, and as a consequence, the core component of Si IV spectra starts growing, as shown by the line profile at $t = 5.4$ s. As smaller plasmoids grow and merge with each other to form larger plasmoids, the core component grows stronger, leading to triangular shaped line profile with a strong core and two broad wings at $t = 13$ s. The temporal evolution of synthetic Si IV spectra from a simulated current sheet agrees well with IRIS observations (Figure 2), suggesting evolving line profiles of the UV bursts presented in this paper are driven by the growth of the plasmoid instability.

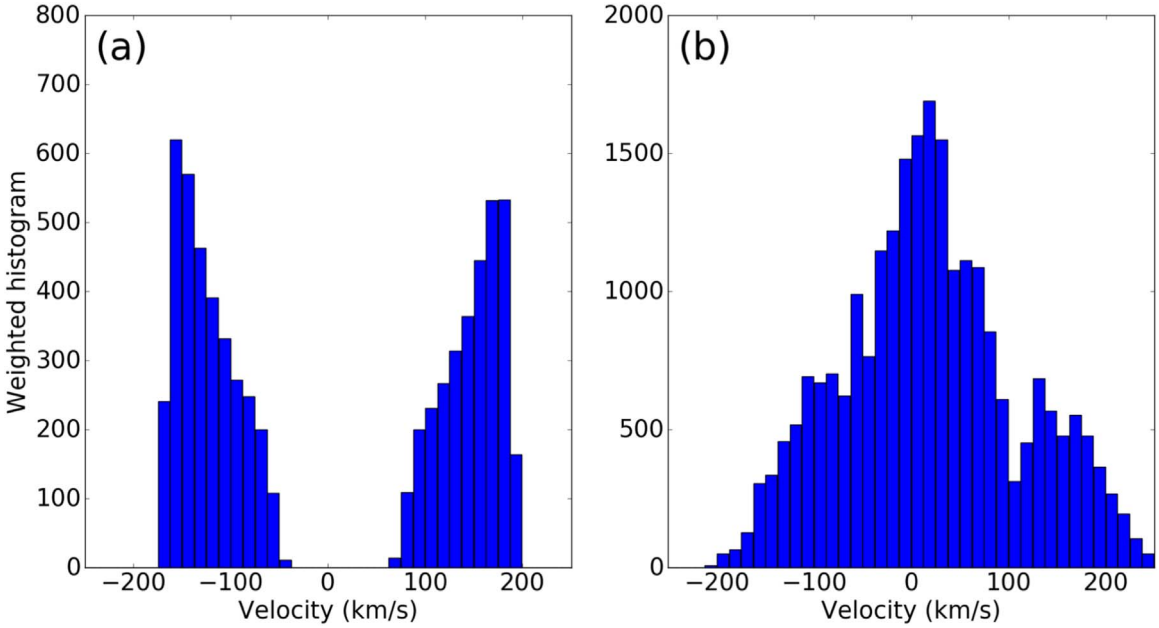

Figure 5. Weighted histogram of the outflow velocity (weighted by the square of the density) in the current sheet during the slow phase (a) and the fast phase (b).

Figure 5 shows histograms of the amount of plasma in different velocity intervals, which will contribute to emission of the Si IV line if the local temperature is close to the formation temperature of Si IV (80,000 K). Panel (a) shows that during the slow phase, the current sheet is dominated by Alfvénic flows in a bidirectional jet, resulting in a double-peaked histogram. The bidirectional jet weakens when plasmoids start to appear in the current sheet. As the plasmoids grow, they cause fluctuations in the density profile of the current sheet. During the fast phase (panel (b)), a substantial number of plasmoids are formed, which move along the current sheet at highly fluctuating velocities. In other words, a substantial amount of plasmoids can move at velocities significantly lower than the Alfvén speed. This result agrees with the numerical experiments reported in Huang & Bhattacharjee (2012), which suggests that plasmoids in the current sheet assume a broad distribution in size and lead to a similar distribution of velocities. The high-speed part of the velocity distribution is the reason for the Doppler-shifted wings on both blue and red sides of the line profiles, which are sometimes mentioned as high-velocity tails of the UV burst spectra, while the low-speed core of the velocity distribution leads to a strong central component in the Si IV spectra.

5. Conclusions and Discussion

In this paper, we present rare spectroscopic observations of the transition of a reconnecting current sheet from a slow quasi-continuous phase to a fast and impulsive phase. We find that the observations of events showing bidirectional flows followed quickly by triangular shaped profiles are compatible with the growth of the plasmoid instability, which is an important prediction of theory but had not yet been validated by experimental or observational evidence until now. While theoretical work on this mechanism has been extensive, observational studies are typically more limited because of practical considerations (e.g., limitations of remote sensing). Thanks to the high temporal resolution and high sensitivity of the IRIS instrument, we can now, for the first time, shed light on the events preceding the impulsive phase of transition region UV bursts or explosive events. The new observations presented here have the special feature of capturing both the slow and the impulsive phases of the events, and the close correspondence with the simulation results makes a compelling case for the interpretation based on the nonlinear plasma instability. These observations, which go further than previous reports (e.g., Innes et al. 1997, 2015; Hara et al. 2011) on plasmoids on the Sun, demonstrate that IRIS spectroscopic data can be used for diagnosing rapid reconnection dynamics on the Sun, thereby opening up opportunities for future studies that constrain theoretical models of magnetic reconnection.

We gratefully acknowledge support by NASA contract NNG09FA40C (IRIS). The simulations have been run on the Pleiades cluster through the computing project s1061 from the High End Computing (HEC) division of NASA. Data are courtesy of IRIS, SDO/AIA, and SDO/HMI. IRIS is a NASA small explorer mission developed and operated by LMSAL with mission operations executed at NASA Ames Research Center and major contributions to downlink communications funded by ESA and the Norwegian Space Centre.

ORCID iDs

L.-J. Guo https://orcid.org/0000-0002-3631-4357
Bart De Pontieu https://orcid.org/0000-0002-8370-952X
Y.-M. Huang https://orcid.org/0000-0002-4237-2211
H. Peter https://orcid.org/0000-0001-9921-0937

References

Bhattacharjee, A., Huang, Y.-M., Yang, H., & Rogers, B. 2009, PhPl, 16, 112102
Bhattacharjee, A., Ma, Z. W., & Wang, X. 2001, PhPl, 8, 1829
Brueckner, G. E. 1981, SSRv, 29, 407
Burch, J. L., Torbert, R. B., Phan, T. D., et al. 2016, Sci, 352, aaf2939
Chen, L. J., Bhattacharjee, A., Puhl-Quinn, P. A., et al. 2008, NatPh, 4, 19
Chitta, L. P., & Lazarian, A. 2020, ApJL, 890, L2
Colgan, J., Abdallah, J., Jr., Sherrill, M. E., et al. 2008, ApJ, 689, 585

Comisso, L., Lingam, M., Huang, Y.-M., & Bhattacharjee, A. 2016, PhPl, 23, 100702
Curdt, W., & Tian, H. 2011, A&A, 532, L9
Curdt, W., Tian, H., & Kamio, S. 2012, SoPh, 280, 417
De Pontieu, B., Title, A. M., Lemen, J. R., et al. 2014, SoPh, 289, 2733
Dere, K. P., Bartoe, J. D. F., & Brueckner, G. E. 1989, SoPh, 123, 41
Dere, K. P., Bartoe, J.-D. F., Brueckner, G. E., Ewing, J., & Lund, P. 1991, JGRA, 96, 9399
Dorfman, S., Ji, H., Yamada, M., et al. 2013, GeoRL, 40, 233
Hansteen, V., Ortiz, A., Archontis, V., et al. 2019, A&A, 626, A33
Hara, H., Watanabe, T., Harra, L. K., Culhane, J. L., & Young, P. R. 2011, ApJ, 741, 107
Harris, E. G. 1962, NCim, 23, 115
Howard, R. A., Vourlidas, A., Bothmer, V., et al. 2019, Natur, 576, 232
Huang, Y.-M., & Bhattacharjee, A. 2012, PhRvL, 109, 265002
Huang, Y.-M., Comisso, L., & Bhattacharjee, A. 2017, ApJ, 849, 75
Huang, Y.-M., Comisso, L., & Bhattacharjee, A. 2019, PhPl, 26, 092112
Hurley, K., Boggs, S., Smith, D., et al. 2005, Natur, 434, 1098
Innes, D. E., Guo, L.-J., Huang, Y.-M., & Bhattacharjee, A. 2015, ApJ, 813, 86
Innes, D. E., Inhester, B., Axford, W. I., & Wilhelm, K. 1997, Natur, 386, 811
Ji, H., Terry, S., Yamada, M., et al. 2004, PhRvL, 92, 115001
Karlický, M., & Bárta, M. 2007, A&A, 464, 735
Kato, Y., Hayashi, M. R., & Matsumoto, R. 2004, ApJ, 600, 338
Katz, N., Egedal, J., Fox, W., et al. 2010, PhRvL, 104, 255004
Kliem, B., Karlický, M., & Benz, A. O. 2000, A&A, 360, 715
Lemen, J. R., Title, A. M., Akin, D. J., et al. 2012, SoPh, 275, 17
Li, L., Zhang, J., Peter, H., et al. 2016, NatPh, 12, 847
Lin, J., & Forbes, T. G. 2000, JGR, 105, 2375
Lin, J., Ko, Y.-K., Sui, L., et al. 2005, ApJ, 622, 1251
Loureiro, N. F., Schekochihin, A. A., & Cowley, S. C. 2007, PhPl, 14, 100703
Lui, A. T. Y. 1996, JGR, 101, 13067
Pesnell, W. D., Thompson, B. J., & Chamberlin, P. C. 2012, SoPh, 275, 3
Peter, H., Huang, Y. M., Chitta, L. P., & Young, P. R. 2019, A&A, 628, A8
Peter, H., Tian, H., Curdt, W., et al. 2014, Sci, 346, 315
Pucci, F., & Velli, M. 2013, ApJL, 780, L19
Rouppe van der Voort, L., De Pontieu, B., Scharmer, G. B., et al. 2017, ApJL, 851, L6
Scherrer, P. H., Schou, J., Bush, R. I., et al. 2012, SoPh, 275, 207
Shibata, K., & Magara, T. 2011, LRSP, 8, 6
Shibata, K., & Tanuma, S. 2001, EP&S, 53, 473
Singh, K. A. P., Isobe, H., Nishizuka, N., Nishida, K., & Shibata, K. 2012, ApJ, 759, 33
Sitnov, M., Birn, J., Ferdousi, B., et al. 2019, SSRv, 215, 31
Takasao, S., Asai, A., Isobe, H., & Shibata, K. 2012, ApJL, 745, L6
Taylor, J. B. 1986, RvMP, 58, 741
Tsuneta, S. 1996, ApJ, 456, 840
Uzdensky, D. A., & Loureiro, N. F. 2016, PhRvL, 116, 105003
Yamada, M., Kulsrud, R., & Ji, H. 2010, RvMP, 82, 603
Young, P. R., Tian, H., Peter, H., et al. 2018, SSRv, 214, 120